RSC Advances

ROYAL SOCIETY OF CHEMISTRY

www.rsc.org/advances

Hollow $NiCo_2S_4$ nanotube arrays grown on carbon textile as self-supported electrode for asymmetric supercapacitors

Liang Hao, Laifa Shen,* Jie Wang, Yunling Xu, and Xiaogang Zhang*

Jiangsu Key Laboratory of Material and Technology for Energy Conversion, College of Material Science & Engineering, Nanjing University of Aeronautics and Astronautics, Nanjing, 210016, P.R. China. Email: lfshen@nuaa.edu.cn, azhangxg@nuaa.edu.cn

Abstract

Although supercapacitors possess the fast charge/discharge capability, the practical application of supercapacitors is still hindered largely by their low energy density. Improving the electrochemical performance of supercapacitors depends largely on development of novel electrode materials and hybrid systems. In this work, hollow $NiCo_2S_4$ nanotube arrays are successfully grown on carbon textile (CT) with robust adhesion through a two-step synthesis, involving the growth of solid nanowire precursor and subsequent conversion into $NiCo_2S_4$ nanotubes by a sulfidation process. Using CT-supported $NiCo_2S_4$ nanotubes arrays as the positive electrode and activated carbon as the negative electrode, a high-performance asymmetric supercapacitor with a maximum voltage of 1.6 V has been fabricated, which manifests high energy density (~40.1 Wh kg^{-1} at 451 W kg^{-1}), high power density (~4725 W kg^{-1} at 21 Wh kg^{-1}) and excellent cycleability.

1 . Introduction

Developing high-performance electrochemical energy storage devices has become one urgent task for scientists and engineers worldwide.[1-4] Among various electric energy storage technologies, supercapacitors have attracted considerable amount of attention due to their high power density, fast charge/discharge capability (in seconds) and exceptionally long cycle life. However, the energy density of commercial supercapacitors (usually less than 10 Wh kg^{-1}) is much lower than that of rechargeable batteries, which greatly limits their practical applications.[5-8] Therefore, one great challenge for the supercapacitor technology is to improve the energy density without sacrificing the power density and cycle life.

According to the equation $E = 1/2CV^2$, the energy density of supercapacitors can be greatly enhanced by maximizing the specific capacitance (C) and/or the cell voltage (V). Recently, designing asymmetric supercapacitors (ASCs) has been regarded as a promising strategy to increase the cell voltage and thus energy density.[9-14] High-energy density ASCs are mostly consisting of a battery-type Faradaic electrode favoring energy density and a capacitive electrode favoring power density. ASCs can allow high output voltage by combing different potential windows of two electrodes, which can in principle lead to a significant improvement of the energy density. The key for developing high-performance ASCs with high power and energy densities relies on development of novel nanostructured electrodes with rational design and compatible electrolyte.

Traditionally, pseudocapacitive transition metal oxides (such as Co_3O_4,[15] NiO,[16] MnO_2[17, 18]) materials are used as positive electrode materials for ASCs. However, one main drawback that restricts the practical application of transition metal oxides is the low electrical conductivity, which usually results in poor rate capability and cycling stability of the cells. Recently, transition metal sulfides such as cobalt sulfides and nickel sulfides have been investigated as a new type of electrode materials for supercapacitors.[19, 20] It is reported that ternary $NiCo_2S_4$ possesses higher electrochemical activity and higher capacitance than corresponding mono-metal sulfides because of the presence of more feasible redox reactions.[21-23] More significantly, $NiCo_2S_4$ exhibits excellent

electrical conductivity that is at least two orders of magnitude higher than that of $NiCo_2O_4$.[24, 25] Several different types of $NiCo_2S_4$ nanostructures, including nanoparticles,[26] nanoplates,[27, 28] nanotubes,[21, 29] microspheres,[24] hollow spheres,[30] and nanocomposites with graphene,[26, 31, 32] have been recently synthesized and their electrochemical performance is investigated. In most cases, nanostructured $NiCo_2S_4$ materials need to be mixed with additives such as binder and carbon black and further pressed onto current collector. This electrode-making process not only causes a large portion of the electroactive $NiCo_2S_4$ surface inaccessible by the electrolyte, but also unavoidably leads to reduced energy density of the device because of the significant weight of auxiliary components.[33] This drawback can partly be overcome by directly growing nanostructured electrode materials on current-collecting substrate.[34] For example, $NiCo_2S_4$ nanostructures have recently been grown on nickel foam. [32, 35, 36] However, nanostructued electrodes supported on metallic current collector are quite rigid in nature, which not only makes the devices less flexible, and more importantly limits the energy density.

In this work, we develop a high-performance ASCs using $NiCo_2S_4$ nanotube arrays (NTAs) grown on CT as the positive electrode and actived carbon (AC) as the negative electrode. $NiCo_2S_4$ NTAs are successfully grown on CT with robust adhesion by a surfactant-assisted hydrothermal method followed by a sulfidation process. The resultant $NiCo_2S_4$/CT hybrid film can directly serve as the additive-free positive electrode for ASCs, which shows high rate capability (1004 F g^{-1} at 20 A g^{-1}) and excellent cycling stability. Remarkably, the ASC based on $NiCo_2S_4$/CT and AC manifests an energy density of 40.1 Wh kg^{-1} at the power density of 451 W kg^{-1}.

2. Experimental Section

Growth of $NiCo_2S_4$ nanotube arrays (NTAs) on Carbon Textile: Carbon textile (CT) was cleaned by ultrasonication in deionized (DI) water, ethanol for 15 min each, and then dried in an oven. In a typical process, 5 mmol of $CoCl_2 \cdot 6H_2O$, 2.5 mmol of $NiCl_2 \cdot 6H_2O$, 2 mmol of hexadecyl trimethyl ammonium bromide, and 9 mmol of urea are dissolved into 50 mL of DI water to form a transparent pink solution. After putting a piece of cleaned carbon cloth (4 cm × 4 cm), the solution was then

transferred to a Teflon-lined stainless steel autoclave and kept at 100 °C. After hydrothermal growth, the carbon textile covered with NiCo-precursor nanowire arrays (NWAs) was taken out and carefully rinsed for several times with deionized water. Then, the NiCo-precursor NWAs grown on CT were immersed in 0.07 M Na_2S solution and kept at 160 °C for 8 h. After cooling down naturally to room temperature, the carbon textile covered with $NiCo_2S_4$ NTAs was taken out and washed with DI water and ethanol for several times, then dried at 60 °C for 12 h. $NiCo_2S_4$ nanotube-assembled urchin-like structures were also prepared in a similar manner without putting carbon textile substrate.

Materials characterization: The crystal structure of the obtained samples was characterized by X-ray diffraction (XRD) (Bruker D8 advance) with Cu Kα radiation. The X-ray photoelectron spectroscopy (XPS) analysis was performed on a Perkin-Elmer PHI 550 spectrometer with Al Kα (1486.6 eV) as the X-ray source. The microstructures were characterized using transmission electron microscopy (TEM) (TEM, FEI, Tecnai-20, USA), high-resolution transmission electron microscopy (HRTEM, JEOL JEM-2010), and field-emission scanning electron microscopy (FESEM, JEOL, JSM-7000). The nitrogen sorption measurement was carried on Autosorb 6B at liquid nitrogen temperature.

Electrochemical measurement: The electrochemical measurements were conducted in a three-electrode electrochemical cell with a Pt counter electrode and a saturated calomel reference electrode in a 6 M KOH solution. The carbon textile-supported $NiCo_2S_4$ NTAs directly served as the working electrode ($NiCo_2S_4$ mass ≈ 1.8 mg cm^{-2}) without any ancillary materials. Besides, the mass percentage of $NiCo_2S_4$ in the final composite is estimated to be 11%. For electrochemical measurements of $NiCo_2S_4$ nanotube-assembled urchin-like structures, the working electrode was prepared by mixing active material, acetylene black and polytetrafluorene-ethylene (PTFE) binder with a weight ratio of 80:15:5. After coating the above slurry on Ni foam, the electrode was dried at 60 °C for 10 h before pressing under a pressure of 10 MPa. The specific capacitance is calculated by the following Equation:

$$C=\frac{I\Delta t}{m\Delta V} \quad (1)$$

where I is the discharge current, Δt is the discharge time, ΔV is the voltage range and m is the mass of the active material.

Supercapacitor devices: Asymmetric supercapacitors (ASCs) were fabricated by assembling $NiCo_2S_4$/CT cathode and AC anode with one piece of cellulose paper as the separator in two-electrode simulation cells. A 6 M KOH solution was employed as the electrolyte. The mass ratio of positive electrode to negative electrode was determined according to the well-known charge balance principle ($q^+ = q^-$). In the relationship, the charge stored by each electrode usually depends on the specific capacitance (C), the potential range for the charge/discharge process (ΔV), and the mass of the electrode (m) described by the following Equation:

$$q = C \times \Delta V \times m \quad (2)$$

In order to obtain $q^+ = q^-$, the mass balancing will be expressed as following Equation 3:

$$\frac{m_+}{m_-} = \frac{C_- \times \Delta V_-}{C_+ \times \Delta V_+} \quad (3)$$

C_+ and C_- are the specific capacitance of the $NiCo_2S_4$/CT and AC electrodes, respectively. ΔV_+ and ΔV_- are the voltage range of one scanning segment (V) of $NiCo_2S_4$/CT and AC electrodes, respectively.

The energy density (E) and power density (P) of ASCs are calculated according to the following equations:

$$E = \frac{\int IV_{(t)}dt}{M} \quad (4)$$

$$P = \frac{E}{\Delta t} \quad (5)$$

Where I is the discharging current, $V_{(t)}$ *is the* discharging voltage excluding the *IR* drop, dt is the time differential, M is the total mass of the active electrode materials, and Δt the discharging time.

If the discharge voltage profiles are approximately linear, Equation (4) can be easily reduced to $E=1/2CV^2$ as usual.

3. Results and Discussion

The growth procedure and resulting electrode architectures are schematically illustrated in **Figure 1** (see the method for the detailed synthesis). Woven by carbon microfibers (Figure S1, see the Supporting Information (SI)), lightweight CT is a unique substrate for controlled growth of $NiCo_2S_4$ NTAs with high flexibility and high conductivity. In the first step, highly ordered Ni-Co precursor nanowire arrays (NWAs) are easily grown on CT under hydrothermal conditions. From the X-ray diffraction (XRD) pattern (Figure S2a, see SI), it is clear that the precursor can be indexed as the (Ni, Co)$(CO_3)_{1/2}OH\cdot 0.11H_2O$ phase.[37] The precursor NWAs grow uniformly on each carbon microfiber to form a large-scale conformal coating with well-established texture structure (Figure S3, see SI). After that, the (Ni, Co)$(CO_3)_{1/2}OH$ precursor is transformed into $NiCo_2S_4$ as confirmed by XRD analysis (Figure S2b, see SI) by reacting with Na_2S under hydrothermal treatment. The accompanying structural evolution from nanowire to nanotube can be ascribed to some diffusion effect, which has been extensively used to synthesize various hollow micro/nanostructures.[38, 39] At the earlier stage of the hydrothermal reacting process, S^{2-} react with metal ions to form a thin layer of Ni–Co sulfides at the surface of the nanowires, which hinder the direct chemical reaction between outside sulfide ions and inner metal-ion species. Then the inner metal ions spontaneously diffuses to the external surface of the nanowires for further chemical reaction and the growth of the $NiCo_2S_4$. The continuous outward diffusion of metal-ion species results in the generation of void space inside the starting nanowires. In comparison, $NiCo_2S_4$ nanotube-assembled urchin-like structures will be formed following the same procedure without the addition of CT substrate (Figure S4, see SI).

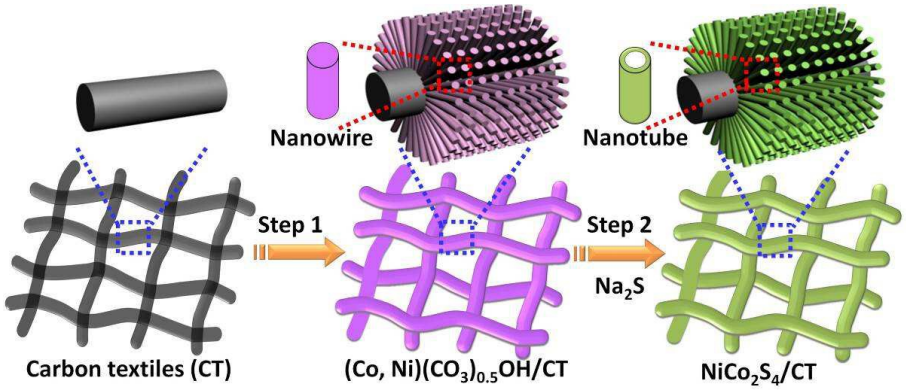

Figure 1. Schematic illustration of the formation of $NiCo_2S_4$ NTAs on CT.

The as-prepared $NiCo_2S_4$/CT composite is characterized by XRD and X-ray photoelectron spectroscopy (XPS). From the XRD pattern (Figure S5, see SI), except the reflections from CT, all other peaks can be indexed to cubic $NiCo_2S_4$ phase (JCPDS card No. 43-1477) although the peak intensity is relatively weak. No residues or impurity phases are detected, indicating that the (Ni, Co)$(CO_3)_{1/2}OH$ precursor is completely converted to $NiCo_2S_4$ phase after sulfidation. The XPS survey spectrum (**Figure 2a**) indicates the presence of Ni, Co, and S, as well as C. By using a Gaussian fitting method, the Co 2p spectrum (Figure 2b) is best fitted with two spin-orbit doublets, characteristic of Co^{2+} and Co^{3+}, and one shake-up satellite (indicated as "Sat."). The Ni 2p spectrum (Figure 2c) is also best fitted with two spin-orbit doublets, characteristic of Ni^{2+} and Ni^{3+}, and two shake-up satellites. The S 2p spectrum (Figure 2d) can be divided into two main peaks and one shake-up satellite. The peak at 163.8 eV, corresponding to S $2p_{3/2}$, is typical of metal–sulfur bonds.[24] The peak at 162.1 eV, corresponding to S $2p_{1/2}$, may be attributed to the S^{2-} in low coordination at the surface. Detailed analysis of the high-resolution spectra shows that the sample contains Co^{2+}, Co^{3+}, Ni^{2+}, Ni^{3+} and S^{2-}, which is in good agreement with the results in literature for $NiCo_2S_4$.[24, 27, 40]

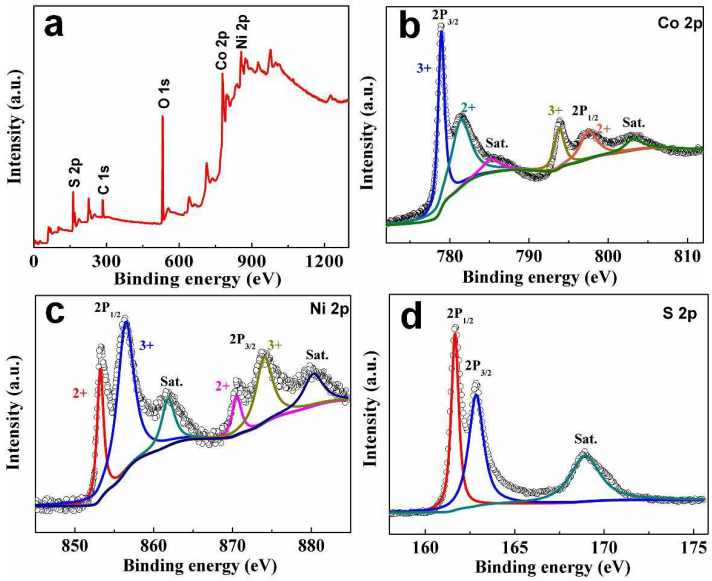

Figure 2. (a) XPS survey spectrum, and high-resolution XPS spectra of (b) Co 2p, (c) Ni 2p and (d) S 2p for the $NiCo_2S_4$ nanotubes scratched from the CT.

After the sulfidation conversion, the formed $NiCo_2S_4$/CT composite still keeps the ordered woven structure of the CT substrate (**Figure 3a**). Inset in Figure 3a shows digital photographs of $NiCo_2S_4$/CT that can be flexed, demonstrating the good flexibility. Figure 3b and 3c show the enlarged scanning electron microscopy (SEM) images of the $NiCo_2S_4$/CT composite. The $NiCo_2S_4$ nanotubes with diameter of 100−150 nm and length of 3−6 μm are grown vertically on the carbon microfiber, which completely retains the array structure of (Ni, Co)$(CO_3)_{1/2}OH$ precursor. The existence of hollow $NiCo_2S_4$ nanotubes is further confirmed by transmission electron microscopy (TEM). As shown in Figure 3d and 3e, a tubular structure is clearly observed with a wall thickness of about 15 nm. Figure 3e reveals that a typical $NiCo_2S_4$ nanotube is actually composed of many small nanoparticles of 10−20 nm in size, which is also confirmed by high-resolution TEM image (Figure 3f). The observed interplanar spacing is measured to be 0.28 and 0.54 nm, which respectively match well with the (311) and (111) lattice planes of $NiCo_2S_4$ phase. As determined by N_2 sorption measurements (Figure S6, see SI), $NiCo_2S_4$ nanotubes possess Brunauer–Emmett–Teller (BET) specific surface area of about 50.2 $m^2\ g^{-1}$ with pore size mostly below 10 nm. The pore may formed by the stacking of nanoparticles. The hollow $NiCo_2S_4$ nanotubes provide larger

surface area (both interior and exterior) and enable facile transport of ions. This will benefit the fast charge transport when used as supercapacitor electrode materials.

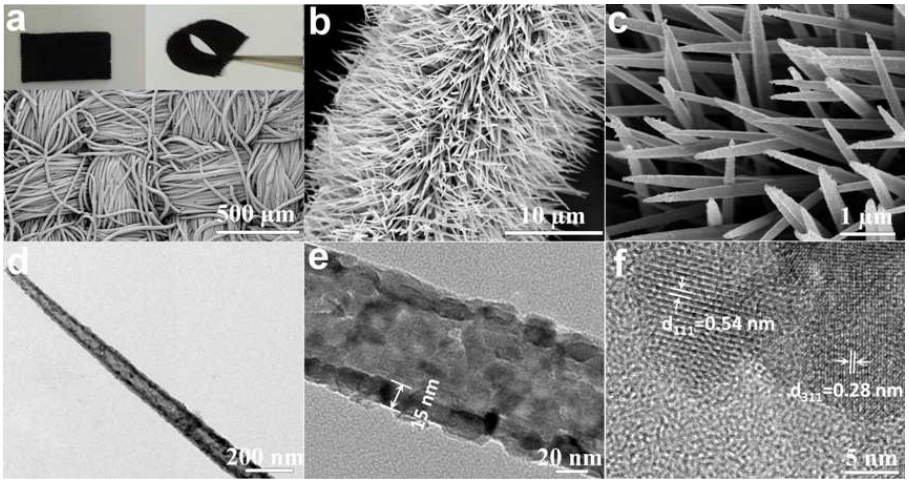

Figure 3. (a, b) Low and (c) high magnification SEM images of the $NiCo_2S_4$/CT composite, showing $NiCo_2S_4$ nanotubes conformally grow on the carbon microfibers. (d, e) Low and (f) high magnification TEM images of one $NiCo_2S_4$ nanotube scratched from the CT.

The electrochemical performance of $NiCo_2S_4$/CT as an additive-free working electrode is first evaluated using a three-electrode cell configuration, and the results are shown in **Figure 4**. Figure 4a shows the cyclic voltammetry (CV) curves of the self-supported $NiCo_2S_4$/CT electrode in a 6 M KOH aqueous electrolyte at various scan rates ranging from 5 to 50 mV s^{-1}. One oxidation peak and two reduction peaks are visible in all CV curves. With the increase in sweep rate from 5 to 50 mV s^{-1}, the general shape of all CV curves evolves insignificantly with some shift in the peak position. These distinct peaks can be attributed to the reversible Faradaic redox processes of $Co^{2+}/Co^{3+}/Co^{4+}$ and Ni^{2+}/Ni^{3+} based on the following reactions:[21, 22]

$$CoS + OH^- \rightleftharpoons CoSOH + e^-$$

$$CoSOH + OH^- \rightleftharpoons CoSO + H_2O + e^-$$

$$NiS + OH^- \rightleftharpoons NiSOH + e^-$$

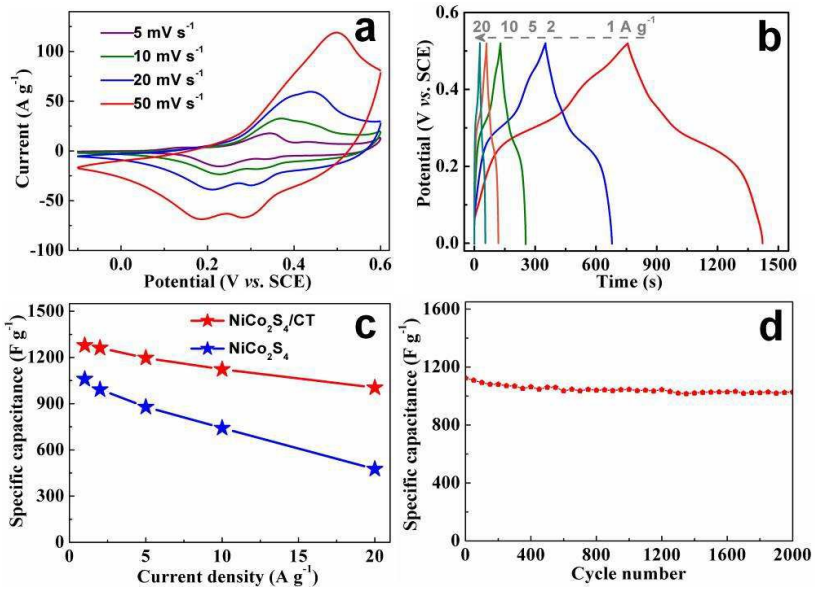

Figure 4. (a) CV curves and (b) Galvanostatic charge/discharge voltage profiles of the $NiCo_2S_4$/CT electrode. (c) Specific capacitance as a function of the current density. (d) Cycling performance of the $NiCo_2S_4$/CT electrode at a current density of 10 A g^{-1}.

Galvanostatic charge/discharge curves of the $NiCo_2S_4$/CT electrode at various current densities ranging from 1 to 20 A g^{-1} are shown in Figure 4b. Consistent with the CV results, the poorly defined voltage plateaus in the charge/discharge curves suggest the presence of some Faradaic processes. The calculated specific capacitance from the discharge curves as a function of the current density is plotted in Figure 4c. Encouragingly, the $NiCo_2S_4$/CT electrode manifests excellent pseudocapacitance of 1279, 1262, 1197, 1123, 1004 F g^{-1} at current densities of 1, 2, 5, 10 and 20 A g^{-1}, respectively. The carbon textile contributes very little capacitance that could be neglected (Figure S7). This means ~78% of the specific capacitance at 1 A g^{-1} is still retained when the discharge current density is increased to 20 A g^{-1}. Compared to the $NiCo_2S_4$/CT electrode, the normal $NiCo_2S_4$ electrode exhibits inferior electrochemical performance when characterized under similar conditions (Figure S8, see SI). As shown in Figure S8a, the CV curves of $NiCo_2S_4$ electrode have been obviously changed. Also shown in Figure 4c for comparison, the specific capacitance of the $NiCo_2S_4$ nanotubes electrode is only 476 F g^{-1} at 20 A g^{-1}, corresponding to only 47.4% of the capacitance achieved by $NiCo_2S_4$/CT electrode at the same current density. A

charge/discharge cycling test at a current density of 10 A g^{-1} is carried out to examine the cycling stability of the $NiCo_2S_4$/CT electrode (Figure 4d). The specific capacitance of the $NiCo_2S_4$/CT electrode decreases from 1123 to 1028 F g^{-1}, corresponding to capacitance retention of ~92% after continuous cycling for 2000 cycles. The above results of high capacitance and excellent rate capability directly reveals the great advantages of $NiCo_2S_4$/CT electrode. The above results also indicate that this rationally designed $NiCo_2S_4$/CT electrode is apparently superior to many other $NiCo_2S_4$ electrodes,[21, 22, 24] and mono-metal sulfides[19, 20, 41, 42] (Table S1, see SI).

To further evaluate the $NiCo_2S_4$/CT electrode for practical applications, an ASC device is fabricated by using the $NiCo_2S_4$/CT electrode as the cathode and the activated carbon (AC) as the anode in a 6 M KOH aqueous electrolyte, with one piece of cellulose paper as the separator. A series of CV and charge/discharge measurements with varying voltage windows is carried out to determine the optimum operating voltage window of the ASC (**Figure 5a and 5b**). With an increase of the operating potential window to 1.6 V, there is more Faradaic reaction observed (the larger current response). Accordingly, the specific capacitance based on the total mass of active materials in both electrodes increases greatly from 52.5 to 98.4 F g^{-1} with the increasing operating potential window from 1.0 to 1.6 V (Figure 5b). It is true that the energy density of supercapacitors can be remarkably improved by increasing the cell voltage. However, when the system is tested at a voltage of 1.8 V or even higher voltages, serious limitation related to electrolysis of water has been observed. Thus, we choose an operating voltage window of 1.6 V to further evaluate the overall electrochemical performance of this optimized ASC.

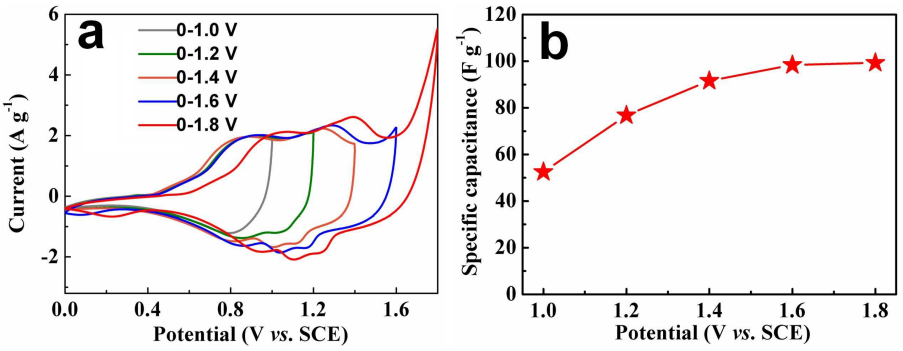

Figure 5. (a) CV curves of $NiCo_2S_4$/CT//AC ASC measured at different potential windows (at 10 mV s^{-1}). (b) Specific capacitance of the ASC with the increase of potential window at a fixed scan rate of 10 mV s^{-1}.

Figure 6a presents the typical CV curves for the optimized $NiCo_2S_4$/CT//AC ASC device at various scan rates between 0 and 1.6 V. From the CV curves, it is clear that both electric double-layer capacitance and pseudocapacitance are significant. There is no obvious distortion in the CV curves even at a high scan rate of 100 mV s^{-1}, indicating the good fast-charge/discharge properties of the device. From the CV curves, the specific capacitance is calculated based on the total mass of active materials in both electrodes, as shown in Figure 6b. The specific capacitance is 111.2 F g^{-1} at a low scan rate of 5 mV s^{-1}. As the scan rate increased from 10 to 20 and 50 mV s^{-1}, the specific capacitance was slightly decreased from 98.4 to 91.5 and 72.9 F g^{-1}, respectively. It should be note that the specific capacitance still retains 59.2 F g^{-1} even at a high scan rate of 100 mV s^{-1}, indicating the excellent rate capability. Galvanostatic charge/discharge curves of the ASC at various current densities are shown in Figure 6c. The charge and discharge curves remain a good symmetry at cell voltage as high as 1.6 V, implying that the cell has excellent electrochemical reversibility and capacitive characteristics. Figure 6d further reveals the outstanding cycle life of the ASC up to 3000 cycles. The specific capacitance retention is ~89.2 % after 3000 cycles at 5 A g^{-1}.

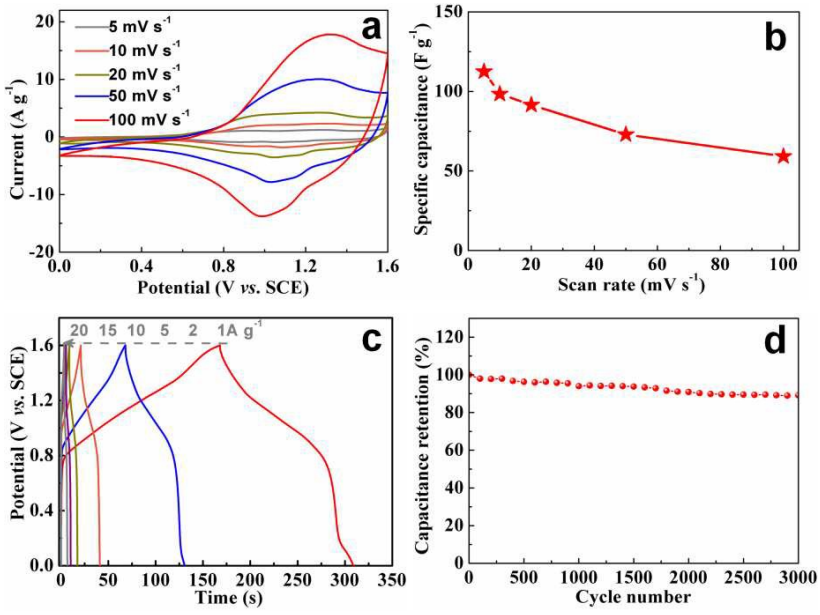

Figure 6. (a) CV curves of ASCs device at various scan rates from 5 to 100 mV s^{-1} measured between 0 and 1.6 V. (b) The specific capacitance as a function of the scan rates. (c) Galvanostatic charge/discharge voltage profiles of the ASC device at different current densities from 1 to 20 A g^{-1}. (d) The specific capacitance of the ASC device as a function of current density. (d) Cycling performance of the ASC device at a current density of 5 A g^{-1}.

We have further evaluated the energy density and power density of the $NiCo_2S_4$/CT//AC ASC based on the total mass of active materials in both electrodes. From the Ragone plot (**Figure 7**), the $NiCo_2S_4$/CT//AC ASC displays a high energy density of 40.1 Wh kg^{-1} at a power density of 451 W kg^{-1}. Even at a high power density of 4725 W kg^{-1}, the ASC still delivers an energy density of 21 Wh kg^{-1}. The superior electrochemical performance of the $NiCo_2S_4$/CT//AC ASC might be attributed to the following design features. The positive electrode structure allows each $NiCo_2S_4$ nanotube to have its own electrical contact with the carbon fiber substrate. The abundant mesopores in the nanotube and large open space between neighboring nanotubes allow facile ion diffusion. This ensures efficient participation of each $NiCo_2S_4$ nanotube in Faradaic electrochemical reactions.

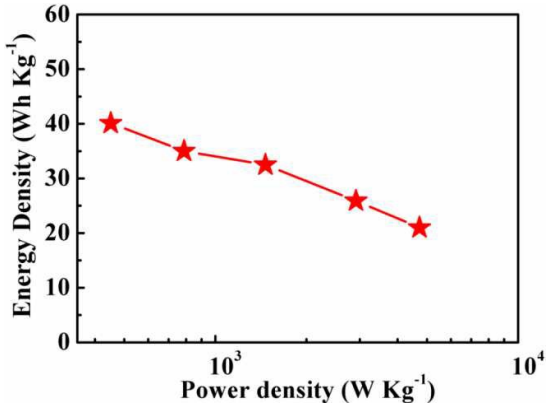

Figure 7. Ragone plots of the ASCs devices based on the total mass of active materials in both electrodes.

4. Conclusion

In summary, we have rationally designed and fabricated an asymmetric supercapacitor using $NiCo_2S_4$ nanotubes arrays on carbon textile as the positive electrode and AC as the negative electrode. The optimal asymmetric supercapacitor device can be reversibly charged and discharged at an operating voltage of 1.6 V in KOH aqueous electrolyte. Importantly, the supercapacitor is able to deliver a high energy density of 40.1 W h kg^{-1} at a power density of 451 W kg^{-1} and a high power density of 4725 W kg^{-1} at an energy density of 21 Wh kg^{-1} (based on the total mass of active materials in both electrodes). The device can retain ~89.2% of the capacitance after 3000 continuous charge/discharge cycles. The present encouraging results show that mixed metal sulfides with high electrochemical activity might be promising for high-performance asymmetric supercapacitors with high voltage, high energy and power densities.

Acknowledgements

This work was supported by the National Basic Research Program of China (973 Program) (No. 2014CB239701), National Natural Science Foundation of China (No. 51372116, 51504139), Natural Science Foundation of Jiangsu Province (BK2011030, BK20150739), the Fundamental Research Funds for the Central Universities (No. NE2016005, NJ20150028).

References

1. J. R. Miller and P. Simon, *Science*, 2008, **321**, 651–652.
2. B. Z. Tian and C. M. Lieber, *Abstr Pap. Am. Chem. S.*, 2009, **238**.
3. S. Chu and A. Majumdar, *Nature*, 2012, **488**, 294–303.
4. G. H. Yu, L. B. Hu, M. Vosgueritchian, H. L. Wang, X. Xie, J. R. McDonough, X. Cui, Y. Cui and Z. N. Bao, *Nano Lett.*, 2011, **11**, 2905–2911.
5. J. S. Huang, B. G. Sumpter and V. Meunier, *Angew. Chem. Int. Edit.*, 2008, **47**, 520–524.
6. X. H. Lu, M. H. Yu, G. M. Wang, T. Zhai, S. L. Xie, Y. C. Ling, Y. X. Tong and Y. Li, *Adv. Mater.*, 2013, **25**, 267–272.
7. W. Fu, C. Zhao, W. Han, Y. Liu, H. Zhao, Y. Ma and E. Xie, *J. Mater. Chem. A*, 2015, **3**, 10492–10497.
8. W. Chen, C. Xia and H. N. Alshareef, *ACS Nano*, 2014, 8, 9531–9541.

9. L. F. Chen, Z. H. Huang, H. W. Liang, Q. F. Guan and S. H. Yu, *Adv. Mater.*, 2013, **25**, 4746–4752.
10. A. Sumboja, C. Y. Foo, X. Wang and P. S. Lee, *Adv. Mater.*, 2013, **25**, 2809–2815.
11. C. L. Long, T. Wei, J. Yan, L. L. Jiang and Z. J. Fan, *ACS Nano*, 2013, **7**, 11325–11332.
12. H. B. Li, M. H. Yu, F. X. Wang, P. Liu, Y. Liang, J. Xiao, C. X. Wang, Y. X. Tong and G. W. Yang, *Nat. Commun.*, 2013, **4**, 1894.
13. Z. Tang, C. H. Tang and H. Gong, *Adv. Funct. Mater.*, 2012, **22**, 1272–1278.
14. X. F. Wang, B. Liu, R. Liu, Q. F. Wang, X. J. Hou, D. Chen, R. M. Wang and G. Z. Shen, *Angew. Chem. Int. Edit.*, 2014, **53**, 1849–1853.
15. C. Zhou, Y. W. Zhang, Y. Y. Li and J. P. Liu, *Nano Lett.*, 2013, **13**, 2078–2085.
16. H. W. Wang, H. Yi, X. Chen and X. F. Wang, *J. Mater. Chem. A*, 2014, **2**, 3223–3230.
17. B. G. Choi, M. Yang, W. H. Hong, J. W. Choi and Y. S. Huh, *ACS Nano*, 2012, **6**, 4020–4028.
18. L. B. Hu, W. Chen, X. Xie, N. A. Liu, Y. Yang, H. Wu, Y. Yao, M. Pasta, H. N. Alshareef and Y. Cui, *ACS Nano*, 2011, **5**, 8904–8913.
19. X. H. Xia, C. R. Zhu, J. S. Luo, Z. Y. Zeng, C. Guan, C. F. Ng, H. Zhang and H. J. Fan, *Small*, 2014, **10**, 766–773.
20. T. Zhu, Z. Y. Wang, S. J. Ding, J. S. Chen and X. W. Lou, *RSC Adv.*, 2011, **1**, 397–400.
21. H. Z. Wan, J. J. Jiang, J. W. Yu, K. Xu, L. Miao, L. Zhang, H. C. Chen and Y. J. Ruan, *Crystengcomm*, 2013, **15**, 7649–7651.
22. L. Yu, L. Zhang, H. B. Wu and X. W. Lou, *Angew. Chem. Int. Ed.*, 2014, **53**, 3711–3714.
23. L. Shen, J. Wang, G. Xu, H. Li, H. Dou and X. Zhang, *Adv. Energy. Mater.*, 2015, **5**. 1400977.
24. H. C. Chen, J. J. Jiang, L. Zhang, H. Z. Wan, T. Qi and D. D. Xia, *Nanoscale*, 2013, **5**, 8879–8883.
25. J. W. Xiao, L. Wan, S. H. Yang, F. Xiao and S. Wang, *Nano Lett.*, 2014, **14**, 831–838.
26. Y. Xiao, D. Su, X. Wang, L. Zhou, S. Wu, F. Li and S. Fang, *Electrochim. Acta*, 2015, **176**, 44–50.
27. J. Pu, F. L. Cui, S. B. Chu, T. L. Wang, E. H. Sheng and Z. H. Wang, *ACS Sustain. Chem. Eng.*, 2014, **2**, 809–815.
28. Z. Wu, X. Pu, X. Ji, Y. Zhu, M. Jing, Q. Chen and F. Jiao, *Electrochim. Acta*, 2015, **174**, 238–245.
29. J. Zhang, H. Gao, M. Zhang, Q. Yang and H. Chuo, *Appl. Surf. Sci.*, 2015, 347, 690–695.

30. L. Shen, L. Yu, H. B. Wu, X.-Y. Yu, X. Zhang and X. W. D. Lou, *Nat. Commun.*, 2015, **6**, 6694.
31. S. J. Peng, L. L. Li, C. C. Li, H. T. Tan, R. Cai, H. Yu, S. Mhaisalkar, M. Srinivasan, S. Ramakrishna and Q. Y. Yan, *Chem. Commun.*, 2013, **49**, 10178–10180.
32. C. Lamiel and J.-J. Shim, *Electrochim. Acta*, 2015, **161**, 351–357.
33. L. Shen, Q. Che, H. Li and X. Zhang, *Adv. Funct. Mater.*, 2014, **24**, 2630–2637.
34. L. F. Shen, E. Uchaker, X. G. Zhang and G. Z. Cao, *Adv. Mater.*, 2012, **24**, 6502–6506.
35. H. Wang, C. Wang, C. Qing, D. Sun, B. Wang, G. Qu, M. Sun and Y. Tang, *Electrochim. Acta*, 2015, **174**, 1104–1112.
36. H. C. Chen, J. J. Jiang, L. Zhang, D. D. Xia, Y. D. Zhao, D. Q. Guo, T. Qi and H. Z. Wan, *J. Power Sources*, 2014, **254**, 249–257.
37. J. W. Xiao and S. H. Yang, *RSC Adv.*, 2011, **1**, 588–595.
38. Y. D. Yin, R. M. Rioux, C. K. Erdonmez, S. Hughes, G. A. Somorjai and A. P. Alivisatos, *Science*, 2004, **304**, 711–714.
39. H. L. Cao, X. F. Qian, C. Wang, X. D. Ma, J. Yin and Z. K. Zhu, *J. Am. Chem. Soc.*, 2005, **127**, 16024–16025.
40. J. Pu, T. T. Wang, H. Y. Wang, Y. Tong, C. C. Lu, W. Kong and Z. H. Wang, *ChemPlusChem*, 2014, **79**, 577–583.
41. H. Pang, C. Z. Wei, X. X. Li, G. C. Li, Y. H. Ma, S. J. Li, J. Chen and J. S. Zhang, *Sci. Rep-Uk*, 2014, **4**, 3577.
42. J. Yang, X. Duan, W. Guo, D. Li, H. Zhang and W. Zheng, *Nano Energy*, 2014, **5**, 74–81.